

Superconvergent Non-Polynomial Approximations *

Andrew J. Christlieb [†]

William A. Sands [‡]

Hyoseon Yang [§]

Abstract

In this paper, we introduce a superconvergent approximation method using a non-polynomial that consists of radial basis functions (RBFs) to solve conservation laws. The use of RBFs for interpolation and approximation is a well developed area of research. Of particular interest in this work is the development of high order finite volume (FV) weighted essentially non-oscillatory (WENO) methods, which utilize RBF approximations to obtain required data at the cell interfaces. Superconvergence of the approximations is addressed through analyses, which result in the attainment of expressions for optimal RBF shape parameters. This study seeks to address the practical elements of the approach, including the evaluations of shape parameters and a hybrid implementation. To highlight the effectiveness of the non-polynomial basis, the proposed methods are applied to one-dimensional hyperbolic and weakly hyperbolic systems of conservation laws. In the latter case, notable improvements are observed in predicting the location and height of the finite time blowup. The convergence results demonstrate that the proposed schemes attain improvements in accuracy, as indicated by the analyses.

Keywords: Superconvergence, radial basis functions, WENO scheme, conservation laws, shape parameter

1 Introduction

This work concerns the development of numerical schemes to solve conservation laws, which are of the form

$$\begin{cases} u_t + \nabla \cdot F(u) = 0, & x \in \mathbb{R}^m, \\ u(x, 0) = u_0(x), \end{cases} \quad (1)$$

where $F(u)$ is the flux function and $u_0(x)$ is the prescribed initial data. The necessity and computational cost of high order numerical methods for the problem (1) have motivated, to a large extent, the development of so-called *superconvergent* approximation schemes. Superconvergent schemes can be broadly defined as those which converge at a rate faster than what is theoretically expected. Henceforth, we shall use this definition when referring to superconvergence for the approximations appearing in this work.

Finite volume (FV) schemes are among the most popular methods used to solve hyperbolic conservation laws. An attractive feature of such schemes is that they evolve cell-average data, which makes the discretization naturally conservative. These conservation properties also make them suitable for use in, for example, adaptive mesh refinement algorithms, where data needs to be frequently transferred between grids within a hierarchy in a conservative manner. While there exist many approaches to obtain high order FV discretizations, we restrict our focus to the class of so-called weighted ENO (WENO) schemes [25, 29], introduced by Jiang and Shu [25], which shall be referred to as classical WENO or WENO-JS. These methods were built on the success, and, in a sense, the limitations of the essentially non-oscillatory (ENO) schemes [21, 22, 35, 36], which employed an adaptive interpolation stencil based on a small set of available candidate points, to construct necessary approximations at cell interfaces. WENO approaches, such as [25], in contrast, make use of all available candidate points in the reconstruction through a convex combination of substencils, so that higher order accuracy is attained in smooth regions. In non-smooth

*Last updated on October 28, 2020. The research of the authors was supported in part by AFOSR grants FA9550-19-1-0281 and FA9550-17-1-0394 and NSF grant DMS 1912183.

[†]Department of Computational Mathematics, Science and Engineering, Michigan State University, East Lansing, MI, 48824, United States; christli@msu.edu.

[‡]Department of Computational Mathematics, Science and Engineering, Michigan State University, East Lansing, MI, 48824, United States; sandswi3@msu.edu.

[§]Department of Computational Mathematics, Science and Engineering, Michigan State University, East Lansing, MI, 48824, United States; hyoseon@msu.edu (corresponding author).

RBFs	$\phi(x)$
Gaussian function	$e^{-(\lambda x)^2}$
Multiquadric	$\sqrt{1 + (\lambda x)^2}$
Inverse quadric	$\frac{1}{1 + (\lambda x)^2}$
Thin-plate spline	$(\lambda x)^2 \log(\lambda x)$

Table 1: Commonly used global radial basis functions ϕ with a shape parameter λ .

regions, WENO reduces to making use of one of the substencils to obtain a properly winded, essentially non-oscillatory approximation. The notion of smoothness among each of the candidate substencils is accessed through a smoothness indicator that makes use of the first and second derivative information for the local approximations to identify non-smooth regions. Several other WENO schemes, which are more robust at shock capturing and generate less dissipation have been proposed in the literature (see e.g., [1, 7, 23, 34]). Traditional WENO schemes were originally designed based on the flux constructed from polynomial interpolations. However, algebraic polynomials are known to have limits in approximating data containing rapid gradients or fast oscillations due to their shift-and-scale invariant property. In order to address this problem, schemes were developed based on both trigonometric [47, 48] and exponential [16, 18] functions in the interpolation basis for ENO and WENO.

This paper proposes to use non-polynomial function approximations by formulating a WENO scheme in terms of a RBF and achieving superconvergence by tuning the available shape or tension parameter. RBFs are widely used as a basis function for multivariate scattered data approximation problems [8, 45, 30], and RBF approximation methods for solving partial differential equations have been developed in a variety of contexts [33, 39], including WENO quadratures [6, 15]. A radial basis function $\phi : \mathbb{R}^d \rightarrow \mathbb{R}$ is defined in the sense that $\phi(x) = \phi(|x|)$, where $|\cdot|$ is the usual Euclidean norm. Because of its definition, the power of the RBF approximation is in its meshless property, which is particularly beneficial in modeling scattered data. Moreover, the basis is flexible, as it can be tuned to incorporate local features of the data through the shape parameter. For a given data set, an approximating function $Af(x)$ with an RBF ϕ can be represented as

$$Af(x) = \sum_{j=1}^M \alpha_j \phi(|x - \xi_j|) \quad (2)$$

where $\{\xi_j : j = 1, \dots, M\}$ is a set of reference points and α_j is a weight associated with $\phi(\cdot - \xi_j)$ for $j = 1, \dots, M$. There are several ways to solve (2) depending on the constraints. For example, assuming $f(\Omega)$ is given, then the constraints satisfy

$$Af(x^*) = f(x^*), \quad \forall x^* \in \Omega, \quad (3)$$

which may represent the solution of an interpolation problem (if $|\Omega| = M$) or an optimization problem ($|\Omega| \neq M$). In Table 1, we provide commonly used global radial basis functions ϕ with a shape parameter λ . We note that the RBF approximation scheme (2) using a Gaussian function as a basis, i.e., $\phi(x) = e^{-(\lambda x)^2}$, has a conceptual resemblance with Gaussian Process (GP) modeling [31, 32], which makes a probabilistic prediction instead of solving a linear system (3). In [31, 32], the authors use GP to solve hyperbolic conservation laws.

The topic of superconvergence admits a vast array of literature. For example, several studies have explored the notion of superconvergence, with Discontinuous Galerkin (DG) methods, on time evolution in ordinary differential equations [2, 3], as well as hyperbolic and convection-diffusion PDEs [9, 10]. In DG schemes, superconvergent behavior can be incorporated into the basis by using information from the exact solution, provided one is available. Spectral methods for PDEs can achieve high order accuracy, when the solutions are analytic, for continuous problems. For PDEs that admit discontinuous solutions, Gibbs phenomenon is known to contaminate solutions, resulting in non-uniform convergence [12]. However, in such instances, high order accuracy can be recovered through the use of certain Gegenbauer polynomial based post-processing techniques [13, 37]. In the literature, non-polynomial based numerical schemes have

successfully demonstrated improvements in accuracy. We refer the interested readers to the papers [15] and [17]. The latter work develops a WENO scheme with a basis consisting of exponential polynomials, while the former proposes an ENO scheme that uses RBF interpolation. The main objective of this paper is to devise a FV scheme that attains superconvergence on a compact (four cell) interpolation stencil by exploiting the shape parameter of the non-polynomial basis (i.e., the RBF). As will be discussed in section 3, the convergence order of the scheme will be determined to be either fifth or sixth order depending on the choice of the shape parameter λ in $\phi(x) = e^{-(\lambda x)^2}$.

The organization of this paper is as follows. In section 2, we begin with a general overview of RBF interpolation. Once we have introduced the interpolation problem, we show, in section 3, how the shape parameter in the RBF basis can be used to obtain a superconvergent approximation. Then, in section 4, we briefly summarize the construction of FV WENO schemes for conservation laws, highlighting, in particular, subsection 4.2, which defines the smoothness indicators employed by the proposed schemes. We then outline the steps used to build a hybrid RBF-WENO scheme in subsection 5.1. Experimental results, collected on a suite of test problems consisting of hyperbolic and weakly hyperbolic systems of conservation laws, are provided in section 6. Finally, in section 7, we briefly summarize the ideas presented in this work.

2 RBF Interpolation

In this section, we provide a brief overview of interpolation with radial basis functions, which shall be useful for introducing our new WENO formulation. Suppose that a continuous function $f : \mathbb{R}^d \rightarrow \mathbb{R}$ is known only at a set of discrete points $X := \{x_1, \dots, x_N\}$ in $\Omega \subset \mathbb{R}^d$. A function $\phi : \mathbb{R}^d \rightarrow \mathbb{R}$ is radial in the sense that $\phi(x) = \phi(|x|)$, where $|\cdot|$ is the usual Euclidean norm. RBF interpolation for f on X starts by choosing a basis function ϕ , and then defines an interpolant by

$$Af_X(x) := \sum_{k=1}^m \beta_k p_k(x) + \sum_{j=1}^N \alpha_j \phi(x - x_j), \quad (4)$$

where $\{p_1, \dots, p_m\}$ is a basis for Π_m and the coefficients α_j and β_i are chosen to satisfy the linear system

$$\left\{ \begin{array}{l} Af_X(x_i) = \sum_{k=1}^m \beta_k p_k(x_i) + \sum_{j=1}^N \alpha_j \phi(x_i - x_j) = f(x_i), \quad i = 1, \dots, N, \\ \sum_{j=1}^N \alpha_j p_k(x_j) = 0, \quad k = 1, \dots, m. \end{array} \right. \quad (5)$$

For a wide choice of functions ϕ and polynomial orders m , the existence and uniqueness of the solution of the linear system (5) is ensured when ϕ is a conditionally positive definite function.

Definition 2.1 Let $\phi : \mathbb{R}^d \rightarrow \mathbb{R}$ be a continuous function. We say that ϕ is conditionally positive definite of order $m \in \mathbb{N}$ if for every finite set of pairwise distinct points $X = \{x_1, \dots, x_N\} \subset \mathbb{R}^d$ and $\alpha = (\alpha_1, \dots, \alpha_N) \in \mathbb{R}^N \setminus \{0\}$ satisfying $\sum_{j=1}^N \alpha_j p(x_j) = 0$ for $\forall p \in \Pi_m$, the quadric form

$$\sum_{i=1}^N \sum_{j=1}^N \alpha_i \alpha_j \phi(x_i - x_j)$$

is positive definite.

This leads to a linear system (5) for $\alpha = (\alpha_1, \dots, \alpha_N)$ and $\beta = (\beta_1, \dots, \beta_m)$, which is given in block-matrix form as

$$\begin{bmatrix} \Phi & P^T \\ P & O \end{bmatrix} \begin{bmatrix} \alpha^T \\ \beta^T \end{bmatrix} = \begin{bmatrix} \mathbf{f}^T \\ O \end{bmatrix} \quad (6)$$

where $\Phi = \{\phi(x_i - x_j) : i, j\}$, $P = \{p_k(x_j) : k, j\}$ and $\mathbf{f} = \{f(x_i) : i\}$. If we assume $m = 0$ in (4), then from the equations (4) and (6), the interpolant can be represented as

$$Af_X(x) = \sum_{j=1}^N \alpha_j \phi(x - x_j) = \Phi \Phi^{-1} \mathbf{f}^T, \quad (7)$$

where $\phi = \{\phi(x - x_j) : j\}$. We note that the product $\phi\Phi^{-1}$, which appears as part of the representation (7), is completely independent of the function values \mathbf{f} . Next, in section 3, expressions for optimal shape parameters λ in the RBF basis are derived, resulting in superconvergent approximations.

3 Superconvergent RBF schemes

In this section, we derive the expressions for optimal shape, or tension, parameters for RBF interpolation. We provide analyses in section 3.1 using two reconstruction methods: a direct approach using integrals and a second approach that utilizes a primitive function. Here, we choose the shape parameter λ , for a given RBF ϕ , so that it improves the convergence order of the interpolation.

3.1 Optimal Shape Parameters for RBFs

In [16], the authors introduced a WENO scheme based on the space of exponential polynomials. Later, in the work [18], they improved the order of accuracy of their schemes by exploiting the control parameter $\lambda \in \mathbb{R}$ or $i\mathbb{R}$ for exponential basis functions of the form $e^{\lambda x}$. We adopt a similar strategy in this work with the difference being the choice of the basis. Here, the basis functions consist of infinitely smooth RBFs ϕ (see Table 1) rather than exponential polynomials. We present detailed analyses using the Gaussian RBF

$$\phi(x) = e^{-\lambda^2 x^2}, \quad \lambda \in \mathbb{R} \text{ or } i\mathbb{R}, \quad (8)$$

for the case of $N = 2$ using two different approaches. For each approach, we provide analytical expressions for the optimal shape parameters, which allow the schemes to achieve superconvergence on a fixed reconstruction stencil.

3.1.1 Direct Computation with Integrals

Recall that the RBF approximation is given by

$$Au(x) := \sum_{k=1}^2 \alpha_k \phi(x - x_{j+k-1}) = \alpha_1 \phi(x - x_j) + \alpha_2 \phi(x - x_{j+1}). \quad (9)$$

The goal is to form a high order approximation using the form (9), which preserves each of the cell averages. In other words, the approximation should satisfy the integral constraint

$$\frac{1}{\Delta x} \int_{I_i} Au(\xi) d\xi = \bar{u}_i, \quad i = j, j+1. \quad (10)$$

Using the RBF $\phi(x)$ defined in (8), it follows that the integrals of ϕ can be evaluated analytically, which resulting in a solvable linear system. Once the solution is determined, the final approximation at the cell boundary $x_{j+\frac{1}{2}}$ is given by

$$Au(x_{j+\frac{1}{2}}) = \frac{2\lambda\Delta x \exp(-\frac{\lambda^2\Delta x^2}{4})}{\sqrt{\pi} \left(\operatorname{erf}(\frac{\lambda\Delta x}{2}) + \operatorname{erf}(\frac{3\lambda\Delta x}{2}) \right)} (\bar{u}_j + \bar{u}_{j+1}).$$

To determine the shape parameter, we Taylor expand the right-hand side of the previous equation, which yields

$$\begin{aligned} Au(x_{j+\frac{1}{2}}) &\approx \left(\frac{1}{2} + \frac{\lambda^2\Delta x^2}{6} - \frac{7\lambda^4\Delta x^4}{90} \right) (\bar{u}_j + \bar{u}_{j+1}) \\ &= u(x_{j+\frac{1}{2}}) + \Delta x^2 \left(\frac{1}{3}\lambda^2 u(x_{j+\frac{1}{2}}) + \frac{1}{6}u''(x_{j+\frac{1}{2}}) \right) + \mathcal{O}(\Delta x^4). \end{aligned}$$

Hence, we have a second order approximation for the cell boundary point. Notice that we can obtain a fourth order approximation if we choose the shape parameter with

$$\lambda^2 = -\frac{u''(x_{j+\frac{1}{2}})}{2u(x_{j+\frac{1}{2}})} + \mathcal{O}(\Delta x^2).$$

In practice, this ratio can be formed using the available cell average data. Derivatives in such expressions are approximated using finite differences, here, although there may be many ways to approximate these terms. Note that the data can be shifted by some positive constant at the beginning and end of the reconstruction steps, to prevent division by zero, if needed. Lastly, if λ^2 is too large, we replace it with a constant whose sign matches λ^2 – the particular value of this constant is not important. In the next section, we perform a similar reconstruction using a primitive function.

3.1.2 Construction with a Primitive Function

To reconstruct the approximation at the cell boundary $x = x_{j+\frac{1}{2}}$ from the cell averages $\{\bar{u}_j, \bar{u}_{j+1}\}$, we define a primitive function

$$U(x) = \int_{x_{j-\frac{1}{2}}}^x u(\xi) d\xi$$

which can be explicitly written in terms of the available cell averages as

$$U(x_{i-1/2}) = \Delta x \sum_{\ell=j}^{i-1} \bar{u}_\ell \quad \text{for } i = j, \dots, j+2.$$

Using the available interpolatory data for the primitive function at the cell interfaces, we seek an RBF representation

$$AU(x) := \sum_{k=0}^2 \alpha_k \phi\left(x - x_{j+k-\frac{1}{2}}\right), \quad (11)$$

which satisfies

$$AU(x_{i-\frac{1}{2}}) = U(x_{i-\frac{1}{2}}), \quad i = j, \dots, j+2. \quad (12)$$

Then the final approximation to $u(x)$ at $x = x_{j+\frac{1}{2}}$ is obtained by differentiating the RBF representation

$$AU'(x) := \sum_{k=0}^2 \alpha_k \phi'(x - x_{j+k-\frac{1}{2}}),$$

which approximates $U'(x) = u(x)$, i.e.,

$$AU'(x_{j+\frac{1}{2}}) \approx U'(x_{j+\frac{1}{2}}) = u(x_{j+\frac{1}{2}}). \quad (13)$$

The approximation based on a Gaussian RBF $\phi(x)$ is found to be

$$AU'(x_{j+\frac{1}{2}}) = 2\lambda^2 \Delta x^2 \frac{e^{3\lambda^2 \Delta x^2}}{e^{4\lambda^2 \Delta x^2} - 1} (\bar{u}_j + \bar{u}_{j+1}), \quad (14)$$

with the basis coefficients calculated from (12) and (13). Applying a Taylor expansion to the right-hand side of this equation gives

$$\begin{aligned} AU'(x_{j+\frac{1}{2}}) &\approx \left(\frac{1}{2} + \frac{1}{2} \lambda^2 \Delta x^2 - \frac{1}{12} \lambda^4 \Delta x^4 \right) (\bar{u}_j + \bar{u}_{j+1}) \\ &= u(x_{j+\frac{1}{2}}) + \Delta x^2 \left(\lambda^2 u(x_{j+\frac{1}{2}}) + \frac{1}{6} u''(x_{j+\frac{1}{2}}) \right) + \mathcal{O}(\Delta x^4). \end{aligned}$$

Hence, we have the second order approximation for the reconstructed cell boundary point. Alternatively, we can obtain the fourth order approximation if we choose the shape parameter with

$$\lambda^2 = -\frac{u''(x_{j+\frac{1}{2}})}{6u(x_{j+\frac{1}{2}})} + \mathcal{O}(\Delta x^2), \quad (15)$$

which can be computed using the techniques previously described at the end of section 3.1.1.

Similarly, we can compute for the case of $N = 4$. Using the cell averages $\{\bar{u}_j : j = -1, \dots, 2\}$, the approximation is defined by

$$AU(x) := \sum_{k=-1}^3 \alpha_k \phi(x - x_{j+k-\frac{1}{2}}) \quad (16)$$

and at the cell boundary $x = x_{j+\frac{1}{2}}$, we have that

$$\begin{aligned} AU(x_{i-\frac{1}{2}}) &= U(x_{i-\frac{1}{2}}) \\ &= \Delta x \sum_{\ell=j}^{i-1} \bar{u}_\ell, \quad i = j-1, \dots, j+3. \end{aligned} \quad (17)$$

Proceeding as before, we can obtain the solution

$$AU'(x_{j+\frac{1}{2}}) \approx \sum_{k=-1}^2 C_k \bar{u}_{j+k} \quad (18)$$

with coefficients C_k computed from equations (16) and (17), and Taylor expand it about the cell boundary $x = x_{j+\frac{1}{2}}$ to find that

$$AU'(x_{j+\frac{1}{2}}) = u(x_{j+\frac{1}{2}}) + \Delta x^4 \left(\frac{1}{30} u^{(4)}(x_{j+\frac{1}{2}}) + \frac{2}{3} \lambda^2 u''(x_{j+\frac{1}{2}}) + 2u(x_{j+\frac{1}{2}}) \lambda^4 \right) + \mathcal{O}(\Delta x^6).$$

Next, we choose λ to remove the $\mathcal{O}(\Delta x^4)$ term, i.e.,

$$\lambda^2 = \frac{-\frac{1}{3} u''(x_{j+\frac{1}{2}}) \pm \sqrt{\frac{1}{9} u''(x_{j+\frac{1}{2}})^2 - \frac{1}{15} u(x_{j+\frac{1}{2}}) u^{(4)}(x_{j+\frac{1}{2}})}}{2u(x_{j+\frac{1}{2}})} + \mathcal{O}(\Delta x^p), \quad (19)$$

which can be computed using the same techniques previously discussed. Therefore we can obtain a superconvergent scheme, which is $(4+p)$ th order accurate with $p \leq 2$.

Theorem 3.1 *Let u be a smooth function on Ω and ϕ is a smooth radial basis function. Given a set of reference points $\{x_k \in \Omega : k = 1, \dots, N\}$ for an even integer N , there exists a set of coefficients $\{\alpha_k : k = 1, \dots, N\}$ of the approximation*

$$Au(x) = \sum_{k=1}^N \alpha_k \phi(x - x_k)$$

to the function $u(x)$, which are constructed from cell averaged data $\{\bar{u}(x_j) : x_j \in \Omega\}$. Moreover, the resulting approximation is $(N+p)$ th order accurate, with $0 \leq p \leq 2$, i.e.,

$$Au(x) = u(x) + \mathcal{O}(\Delta x^{N+p}),$$

for $x \in \Omega$.

The proof of this theorem is inductive and is a relatively direct construction, as in the cases provided above. In this paper, we only supply the proper shape parameters for the case where N is even. However, note that the analysis can be applied to odd values of N , which is provided in appendix A. We now proceed to the discussion of WENO schemes in section 4, making use of the superconvergent RBF approximations.

4 WENO Schemes

This section describes the general formulation of FV WENO schemes used to solve conservation laws. First, we provide a brief summary of the FV discretization in section 4.1. Then, in section 4.2, we introduce new smoothness indicators, which were motivated by numerical experimentation, and discuss the mapping for the WENO weights.

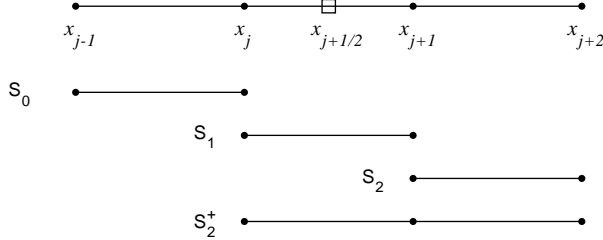


Figure 1: Three two-point substencils S_k , $k = 0, 1, 2$ and a three-point substencil S_2^+

4.1 Formulation of a Finite Volume Scheme

Consider 1D variant of (1), which takes the form

$$\begin{aligned} u_t + f(u)_x &= 0, \quad x \in \mathbb{R}, \\ u(x, 0) &= u_0(x). \end{aligned} \quad (20)$$

To develop a FV discretization, we let the computational domain be uniformly partitioned into cells, so that the j th cell is given by $I_j = [x_{j-1/2}, x_{j+1/2}]$. Further, since the cells are uniformly spaced, each has the size $\Delta x = x_{j+1/2} - x_{j-1/2}$. FV schemes require cell averages of the solution u

$$\bar{u}_j(t) := \frac{1}{\Delta x} \int_{I_j} u(x, t) dx, \quad (21)$$

where the integrals in (21) can be numerically approximated through quadrature of suitable accuracy. By integrating the (20) over the control volume I_j , one obtains a collection of evolution equations defined in each of the control volumes, i.e.,

$$\frac{d}{dt} \bar{u}_j(t) = -\frac{1}{\Delta x} (f(u(x_{j+1/2})) - f(u(x_{j-1/2}))). \quad (22)$$

Defining the numerical flux $\hat{f}_{j\pm 1/2}$ by

$$\hat{f}_{j\pm 1/2} = h(u_{j\pm 1/2}^-, u_{j\pm 1/2}^+), \quad (23)$$

the equation (22) is approximated as

$$\frac{d}{dt} \bar{u}_j(t) = -\frac{1}{\Delta x} (\hat{f}_{j+1/2} - \hat{f}_{j-1/2}). \quad (24)$$

The monotone flux h satisfies several properties, namely, it is Lipschitz continuous in both arguments and should be consistent with the physical flux f , i.e., $h(u, u) = f(u)$. Moreover, the flux should be non-decreasing (non-increasing) with respect to the first (second) argument. In this paper, we employ the HLLC and Lax-Friedrich fluxes for solving the hyperbolic system and the Godunov flux for the weakly hyperbolic system. Definitions of these numerical fluxes can be found in section 6. Next, we focus on the WENO component of the proposed schemes, which seeks to develop high order reconstructions for the cell average data supplied to the numerical flux functions, i.e., $u_{j\pm 1/2}^-$ and $u_{j\pm 1/2}^+$.

4.2 Construction of New Smoothness Indicators

It is well known that the smoothness indicator plays a pivotal role in the WENO reconstruction procedure. The proposed WENO scheme is constructed using three two-point substencils (S_0, S_1, S_2 in Figure 1) so that only the first-order difference operator can be used to estimate the smoothness of numerical fluxes. Therefore, it has some limitations in capturing highly oscillatory structures and rapid gradients, especially on coarse grids. Through experimentation, we also found that switching to the smoothness indicators used in classical WENO (i.e., WENO-JS) resulted in minimal improvement.

In an effort to amend this issue, we employ difference operators which have so-called *exponentially vanishing moments*. The basic idea is that difference operators are constructed so that their applications to smooth functions result in more rapid convergence to zero than classical undivided differences. Such operators should be more effective at detecting smoothness, or lack thereof, in the data, even on a small

collection of points. Before proceeding, we first introduce some ideas from a recent work [17], in which smoothness indicators were constructed using exponential polynomials.

Exponential polynomials can be characterized as the kernel of an operator $p_m(D)$ of the form

$$p_m(D)f := \prod_{i=1}^m (D - \gamma_i I)f, \quad (25)$$

where D is a continuous differential operator, I is an identity operator and $\gamma_i \in \mathbb{C}$, which is associated with the target exponential polynomials. Then, the operator $p_m(D)f$ is constructed as a differential operator which annihilates exponential polynomials. For our purposes, it suffices to consider the case $m = 1$ in equation (25). To illustrate, consider the exponential function $f(x) = e^{-\gamma x}$ for some constant γ . Then, the first order operator $p_1(D)$ with the form $p_1(D)f = (D + \gamma I)f$ annihilates the exponential function, i.e.,

$$f(x) = e^{-\gamma x} \implies p_1(D)f = 0.$$

For the discretized version, we assume the function values $\{f(x_{i-1}), f(x_i)\}$ on the stencil $\{x_{i-1}, x_i\}$ are available. Then, the discrete version of $p_1(D)f$ is defined as

$$\mathbf{p}_1(D)_i f := (D + \gamma I)_i f := e^{\gamma \Delta x} f(x_i) - f(x_{i-1}),$$

which also annihilates the exponential function. Similar constructions can be achieved for $m \geq 2$, leading to m th order operators, which annihilate m exponential polynomials. We refer interested readers to [17].

We are now ready to propose new smoothness indicators based on the new undivided difference with exponentially vanishing moments. Specifically, we define β_k , $k = 0, 1, 2$, by

$$\begin{aligned} \beta_0 &:= |D_{i-1}^1 f|^2 + |\mathbf{p}_1(D)_{i-1} f|^2 = |f_i - f_{i-1}|^2 + |e^{\gamma_i \Delta x} f_i - f_{i-1}|^2, \\ \beta_1 &:= |D_i^1 f|^2 + |\mathbf{p}_1(D)_i f|^2 = |f_{i+1} - f_i|^2 + |e^{\gamma_{i+1} \Delta x} f_{i+1} - f_i|^2, \\ \beta_2 &:= \frac{1}{2} (\beta_1 + (|D_{i+1}^1 f|^2 + |\mathbf{p}_1(D)_{i+1} f|^2)) \\ &= \frac{1}{2} (|f_{i+1} - f_i|^2 + |e^{\gamma_{i+1} \Delta x} f_{i+1} - f_i|^2 + |f_{i+2} - f_{i+1}|^2 + |e^{\gamma_{i+2} \Delta x} f_{i+2} - f_{i+1}|^2). \end{aligned} \quad (26)$$

In smooth regions, β_k should be small, so we select the parameter γ_i in a way that depends on the given stencil data:

$$\gamma_{i+\nu} \Delta x = -\frac{f_{i+\nu} - f_{i+\nu-1}}{f_i + \delta}, \quad \text{sign}(\delta) := \text{sign}(f_i), \quad \nu \in \{0, 1, 2\}. \quad (27)$$

where $\delta = \delta(\Delta x)$ is introduced to prevent the denominator from becoming zero. Observe that β_2 is defined using three points (S_2^+ in Figure 1) instead of two points, which incorporates a bias in the indicators.

Next, using the local smoothness indicators, we map the linear weights d_k to the nonlinear weights α_k for $k = 0, 1, 2$ via

$$\alpha_k = d_k \left(1 + \frac{\tau_3}{\beta_k + \varepsilon} + \left(\frac{\beta_k}{\tau_3 + \varepsilon} \right)^2 \right), \quad \varepsilon := \varepsilon(\Delta x) \quad (28)$$

where $\tau_3 = |\beta_2 - \beta_0|$ measures the global smoothness and $\varepsilon > 0$ is used to prevent the denominator from becoming zero. The linear weights $\{d_k : k = 0, 1, 2\}$ are chosen so that the linear combination of fourth order local approximations, on each of the two-point stencils, is consistent with the sixth order approximation obtained on the four-point stencil. The nonlinear weights are then scaled to form a partition of unity

$$\omega_k = \frac{\alpha_k}{\sum_{\ell=0}^2 \alpha_\ell}, \quad k = 0, 1, 2. \quad (29)$$

The value $u_{j+1/2}^-$ is approximated by a convex combination of local approximations over each of the substencils S_k , $k = 0, 1, 2$ using the nonlinear weights

$$u_{j+1/2}^- = \sum_{k=0}^2 \omega_k u_{j+1/2}^{(k)}.$$

The analogous construction for $u_{j+1/2}^+$ follows by symmetry. In the next section, we present our full FV RBF-WENO algorithm and some details concerning the hybrid implementation.

5 Implementing Superconvergent RBF-WENO Schemes

Now that we have introduced the components of our method (see sections 3 and 4), we can describe the full implementation. First, we begin with some details concerning the hybrid implementation in section 5.1, before addressing the WENO component in section 5.2.

5.1 Comments on the Hybrid Implementation

The implementation of the WENO method used in this work employs a hybrid strategy, which aims to alleviate the computational cost associated with WENO methods due to the additional cost from smoothness indicators and mappings for the nonlinear weights. The basic idea of a hybrid approach is to use reconstructions on a fixed set of cell average data in regions where the data is smooth, while non-smooth regions are appropriately handled with a WENO scheme (see e.g., section 4). The adaptive selection of a reconstruction method relies on the use of certain smoothness criterion, which are, ideally, inexpensive to evaluate. This criterion can, for example, be evaluated with smoothness indicators, such as those in the classical WENO approach [25], as well as divided or undivided differences. A tolerance (or threshold) then selects the reconstruction method according to the smoothness of the given data. Our selection process consists of the following steps:

1. Using finite differences, first compute the relative smoothness $r(x_i)$, which we define as

$$r(x_i) = \frac{2 \left(\left| \delta[\bar{u}](x_i) \right| + \left| \delta^2[\bar{u}](x_i) \right| \right)}{\left| \Delta^-[\bar{u}](x_{i-1}) \right| + \left| \delta^2[\bar{u}](x_{i-1}) \right| + \left| \Delta^+[\bar{u}](x_{i+1}) \right| + \left| \delta^2[\bar{u}](x_{i+1}) \right|}, \quad i = 1, \dots, N, \quad (30)$$

where δ and δ^2 are central difference operators for first and second derivatives, and Δ^- and Δ^+ are the backward and forward difference operators for the first derivative. These difference approximations are all computed with second order accuracy. Note that along the boundaries, data from an extension is required and can be constructed using extrapolation of sufficient accuracy.

2. Once step 1 is complete, we find the minimum and maximum values of the relative smoothness r_{min} and r_{max} and then compute the tolerance

$$r_{tol} = \min \left(\theta, \kappa \frac{r_{min} + \epsilon}{r_{max} + \epsilon} \right). \quad (31)$$

All numerical experiments in this work use $\theta = 1.5$, $\kappa = 5$, and $\epsilon = 1 \times 10^{-10}$.

3. Next, we map $r(x_i) \mapsto \{0, 1\}$ using the previously computed tolerance r_{tol} . We identify cells, which are to use WENO reconstructions, as those for which $r(x_i) \geq r_{tol}$, using fixed stencil reconstructions for those that remain. To account for shortcomings in the definition of the relative smoothness (30), we flag a buffer zone of 4 cells in each direction around any cell marked for WENO reconstruction.

The parameter choices used for θ and κ are based on numerical experimentation and are, by no means, exhaustive. So, there may be better choices for these parameters. Experimentation with different parameters mostly resulted in a more conservative hybrid algorithm, where the WENO reconstruction process was being applied in larger regions of the domain, even where the solution is smooth. While such selections were not particularly detrimental to the shock-capturing abilities of the method, the resulting imbalance does increase the time-to-solution, as the WENO reconstruction is more expensive.

5.2 The FV RBF-WENO Component

Once a method for each cell has been selected, the algorithm then applies the corresponding reconstruction technique. As discussed in the previous section, cells deemed smooth use a four-point fixed stencil RBF interpolant; regions characterized as “non-smooth” apply the RBF-WENO algorithm, which proceeds as follows:

1. Using (14), form the local approximations $u_{j+1/2}^{(k)}$ on each of the two-point substencils $S_k := \{x_{j+k-1}, x_{j+k}\}$, with $k = 0, 1, 2$:

$$u_{j+1/2}^{(k)} := \sum_{\ell=0}^1 c_{\ell}^k \bar{u}_{j+k-1+\ell}.$$

The coefficients c_ℓ^k , where $\ell = 0, 1$ and $k = 0, 1, 2$, are defined with the local shape parameter for the RBF $\phi(x) = \exp(-\lambda_L^2 x^2)$ obtained from (15):

$$\lambda_L^2 \approx -\frac{u''(x_{j+\frac{1}{2}})}{6u(x_{j+\frac{1}{2}})}.$$

Here the function values are replaced with cell averages and the derivatives are obtained with finite differences.

2. Using (18), we can form the approximation $u_{j+1/2}^{S_4}$ on the big stencil $S_4 := \{x_{j-1}, \dots, x_{j+2}\}$ as

$$u_{j+1/2}^{S_4} = \sum_{\ell=-1}^2 C_\ell \bar{u}_{j+\ell},$$

where C_ℓ , and $\ell = -1, \dots, 2$ is a coefficient which is dependent on the global shape parameter λ_G . For the RBF $\phi(x) = \exp(-\lambda_G^2 x^2)$, this is reflected in (19):

$$\lambda_G^2 \approx \frac{-\frac{1}{3}u''(x_{j+\frac{1}{2}}) \pm \sqrt{\frac{1}{9}u''(x_{j+\frac{1}{2}})^2 - \frac{1}{15}u(x_{j+\frac{1}{2}})u^{(4)}(x_{j+\frac{1}{2}})}}{2u(x_{j+\frac{1}{2}})},$$

As in step 1, the function values are replaced with cell averages and the derivatives are obtained with finite differences.

3. Compute the linear WENO weights $\{d_k : k = 0, 1, 2\}$ which satisfy

$$\sum_{k=0}^2 d_k u_{j+1/2}^{(k)} = u_{j+1/2}^{S_4} + O(\Delta x^p),$$

using an appropriate high order p from step 1 and step 2. This results in weights of the form

$$d_0 = \frac{C_{-1}}{c_0^0}, \quad d_2 = \frac{C_2}{c_1^2}, \quad d_1 = 1 - d_0 - d_2.$$

This reflects the partition of unity for the linear weights.

4. Using the cell averages, compute the parameters (27) and the smoothness indicators (26).
5. Map the linear weights $\{d_k : k = 0, 1, 2\}$ from step 3 to nonlinear weights $\{\omega_k : k = 0, 1, 2\}$ using equations (28) and (29).
6. Obtain the reconstructed value at the cell interface using the nonlinear weights:

$$u_{j+1/2}^- = \sum_{k=0}^2 \omega_k u_{j+1/2}^{(k)}.$$

The procedure for determining $u_{j+1/2}^+$ follows, analogously, by reflecting the cell average stencil data. Once the reconstructions for $u_{j+1/2}^\pm$ are completed, we simply apply the numerical flux function (23), which yields $\hat{f}_{j+1/2}$. In the case of hyperbolic systems, these reconstructions are performed component-wise on the characteristic variables.

6 Numerical Results

In this section, we provide some experimental results that demonstrate the improvements offered by the non-polynomial basis. We begin by investigating the performance of the method on some classical 1D test problems for the Euler equations before testing the method on the more challenging pressureless Euler system, which is weakly hyperbolic. All test problems use a third order explicit strong-stability preserving Runge-Kutta method [51] for time integration. In our experiments, we compute the cell average values, from the initial conditions, using high-order Gauss-Legendre quadrature.

6.1 Hyperbolic System

We now present numerical results for the 1D Euler equations of gas dynamics

$$U_t + F(U)_x = 0, \quad (32)$$

where V and $F(V)$ are given as

$$\begin{aligned} U &= (\rho, \rho u, E)^T, \\ F(U) &= (\rho u, \rho u^2 + p, u(E + p))^T. \end{aligned}$$

Here ρ, p, u and E are the density, pressure, velocity, and total energy, respectively. Additionally, we use the equation of state

$$p = (\gamma - 1)(E - \frac{1}{2}\rho u^2), \quad c = \sqrt{\frac{\gamma p}{\rho}},$$

with $\gamma = 1.4$. Here, c denotes the local speed of sound in the gas.

All test problems for the hyperbolic system use the HLLC Riemann solver [41] to compute the flux. Following [52], the HLLC flux is of the form

$$h(U_l, U_r)^T = \begin{cases} F(U_l), & \text{if } s^- \geq 0, \\ F_l^*, & \text{if } s^* \geq 0 \geq s^-, \\ F_r^*, & \text{if } s^+ \geq 0 \geq s^*, \\ F(U_r), & \text{if } s^+ \leq 0, \end{cases} \quad (33)$$

where the intermediate velocity is defined as

$$s^* = \frac{p_r - p_l + \rho_l u_l (s^- - u_l) - \rho_r u_r (s^+ - u_r)}{\rho_l (s^- - u_l) - \rho_r (s^+ - u_r)}.$$

Estimates for the minimum and maximum wave speeds given, respectively, by

$$s^- = \min(u_l - c_l, u_l, u_l + c_l), \quad s^+ = \min(u_r - c_r, u_r, u_r + c_r).$$

Using the Roe pressure

$$p_{lr} = \frac{p_r + p_l + \rho_l (s^- - u_l) (s^* - u_l) + \rho_r (s^* - u_r) (s^+ - u_r)}{2},$$

we form the intermediate fluxes F_l^* and F_r^*

$$F_l^* = \frac{s^* (s^- u_l - F(U_l)) + s^- p_{lr} (0, 1, s^*)^T}{s^- - s^*}, \quad F_r^* = \frac{s^* (s^+ u_r - F(U_r)) + s^- p_{lr} (0, 1, s^*)^T}{s^+ - s^*}.$$

In the case of the Shu-Osher problem (see Example 6.4), we also compared the results of the HLLC flux with the far simpler global Lax-Friedrichs flux

$$h(U_l, U_r)^T = \frac{F(U_l) + F(U_r)}{2} - \alpha \frac{U_r - U_l}{2}. \quad (34)$$

The global dissipation constant α is taken as

$$\alpha = \max_u \max_j |\lambda_j(u)|,$$

with $\lambda_j(u)$ denoting the j th eigenvalue of the flux Jacobian.

Example 6.1 First, we consider the smooth advection problem. Using the initial data

$$\rho(x) = 1 + 0.5 \sin(4\pi x),$$

along with the selections $u = 1$, and $p = 1$, the system reduces to a single advection equation, subject to periodic boundary conditions. The exact solution on $[0, 1]$ is given by

$$\rho(x, t) = 1 + 0.5 \sin(4\pi(x - ut)).$$

In Table 2, we present both the numerical errors and convergence orders of the proposed scheme. When setting the shape parameter λ for the RBF $\phi = e^{-\lambda^2 x^2}$, the approximations in (19) were computed to first and second order accuracy (i.e., $p = 1$ and 2 in (19)). These choices are reflected under the respective labels ‘‘Proposed I’’ and ‘‘Proposed II’’ shown in Table 2. The results demonstrate the expected improved convergence through the choice of the shape parameter.

	N_x	WENO-JS5	Proposed I	Proposed II
L_∞	20	1.17e-02 (—)	3.12e-03 (—)	3.03e-04 (—)
	40	6.95e-04 (4.07)	1.02e-04 (4.94)	5.70e-06 (5.73)
	80	2.61e-05 (4.74)	3.21e-06 (4.99)	8.71e-08 (6.03)
	160	8.70e-07 (4.91)	1.00e-07 (5.00)	1.39e-09 (5.97)
	160	2.68e-08 (5.02)	3.14e-09 (5.00)	2.16e-11 (6.01)
L_1	20	8.14e-03 (—)	1.60e-03 (—)	1.61e-04 (—)
	40	3.74e-04 (4.45)	5.29e-05 (4.92)	3.31e-06 (5.61)
	80	1.18e-05 (4.98)	1.68e-06 (4.98)	5.31e-08 (5.96)
	160	3.69e-07 (5.00)	5.27e-08 (5.00)	8.39e-10 (5.98)
	160	1.15e-08 (5.00)	1.65e-09 (5.00)	1.31e-11 (6.00)

Table 2: (Example 6.1) L_∞ and L_1 errors and convergence rates(*) at $t = 1$.

Example 6.2 We test our method using the Lax problem [28] with the initial condition

$$(\rho, u, p) = \begin{cases} (0.445, 0.698, 3.528) & \text{if } x \in [-5, 0), \\ (0.50, 0, 0.571) & \text{if } x \in [0, 5]. \end{cases}$$

The numerical results for the density profiles are displayed in Figure 2 at time $t = 1.3$ using $\Delta x = 10/200$. The approximation (19) was computed to second order accuracy. The method provides a slight improvement over standard WENO in the context of the Lax problem; although, we expected that the non-polynomial bases, in this case, the Gaussian RBF, would lead to sharper interfaces. As will be seen for finite time blow up problems, or problems with rapid transitions, such as the Shu-Osher dam break problem, the method does give improved results. We hypothesize that more compact representations will provide improvements. This is something we seek to address in a subsequent paper.

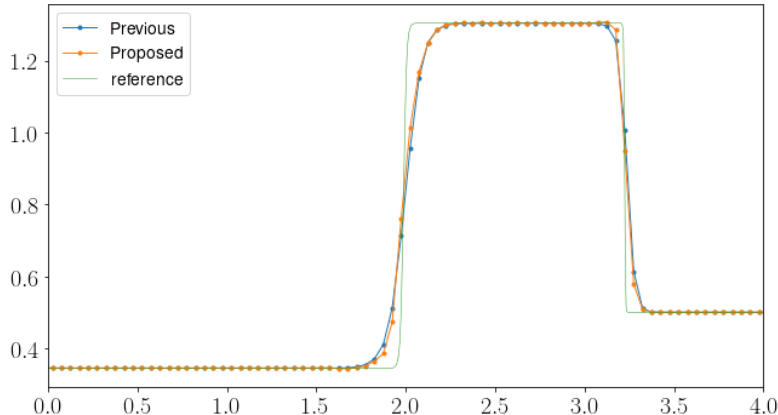


Figure 2: (Example 6.2) Density profiles of Lax problem [28] at $t = 1.3$ with $\Delta x = 10/200$

Example 6.3 As a next example, let us consider the Sod problem [38] with the initial condition

$$(\rho, u, p) = \begin{cases} (1.000, 0.750, 1.000) & \text{if } x \in [0, 0.5), \\ (0.125, 0.000, 0.100) & \text{if } x \in [0.5, 1]. \end{cases}$$

The numerical results for density profiles are given in Figure 3 at time $t = 0.2$ using $\Delta x = 1/100$. Here, we observe results which are similar to the Lax problem (see Example 6.2). As noted above, we plan to investigate these shortcomings in our continued developments of RBF-WENO methods.

Example 6.4 We now look at the Shu-Osher dam brake problem, which uses Riemann initial data for the shock entropy wave interaction [36]. The approximate solutions are computed on the interval $[-5, 5]$

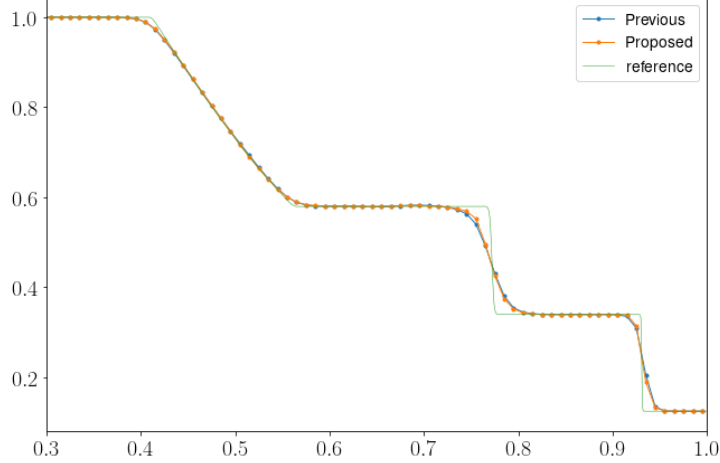


Figure 3: (Example 6.3) Density profiles of Sod problem [38] at $t = 0.2$ with $\Delta x = 1/100$

with the initial state

$$(\rho, u, p) = \begin{cases} (3.857143, 2.629369, 10.33333) & \text{if } x \in [-5, -4), \\ (1 + \varepsilon \sin(kx), 0, 1) & \text{if } x \in [-4, 5], \end{cases} \quad (35)$$

where k and ε denote the wave number and amplitude of the entropy wave respectively. We take $k = 5$ and $\varepsilon = 0.2$ in our experiments.

Figure 4 shows the profiles of the density at time at $t = 1.8$. While the rise time is about the same as the classical WENO method at the shock location, the method is an improvement over standard approaches, as observed in the more rapidly oscillating regions. This improvement stems from the high order nature of the method, in regions away from the shock, where we make use of the optimal shape parameter. We confirmed this hypothesis by testing the method without using the optimal shape parameter. While all of the short-wavelength extrema are well-captured, we do observe undershoots and overshoots in the region immediately behind the shock. In particular, we note the appearance of a saw-tooth-like structure appearing at the shock front. While this structure is, at best, poorly resolved by the classical WENO method, it is readily apparent in the profile for the proposed method. Additionally, the offset in the location of this structure for the proposed scheme can likely be rectified by slightly increasing the cell resolution. Since the proposed scheme utilizes two-point substencils, we do expect some limitations in capturing rapidly varying solutions. Using three (or more) points in the substencils for constructing local solutions would further reduce the undershoot and overshoot.

As previously mentioned, we used both the HLLC flux (Figure 4a) and the global Lax-Friedrichs flux (Figure 4b) in this test problem. It is generally known that the Lax-Friedrichs flux, while simpler to evaluate, produces excessive dissipation – particularly in low order schemes – compared to more intricate Riemann solvers that are more finely tuned to the underlying problem. Our comparison of these Riemann solvers does reflect these observations. In future work, we could use the local version of the Lax-Friedrichs flux, or, perhaps, allow the dissipation to vary by individual quantity, e.g., density, momentum, and energy.

Example 6.5 In [40], Titarev and Toro suggested the following Riemann initial data for the shock entropy wave interaction:

$$(\rho, u, p) = \begin{cases} (1.515695, 0.523346, 1.80500) & \text{if } x \in [-5, -4.5), \\ (1 + 0.1 \sin(20\pi x), 0, 1) & \text{if } x \in [-4.5, 5]. \end{cases}$$

on the interval $[-5, 5]$. Figure 5 shows the results for this test case at time at $t = 5$. This problem allows us to test the method in environments that support highly oscillatory structures. Compared to the Shu-Osher problem (see Example 6.4), the prescribed initial density exhibits a higher wave number, i.e., 20. We find that the results are fairly similar to those obtained in the Shu-Osher problem, in capturing complex wave patterns. While there is a clear improvement in capturing the features of the small wavelength oscillations, we do note the slight undershoot and overshoot in the vicinity of $x = -1.9$, where the transition into the oscillatory region occurs.

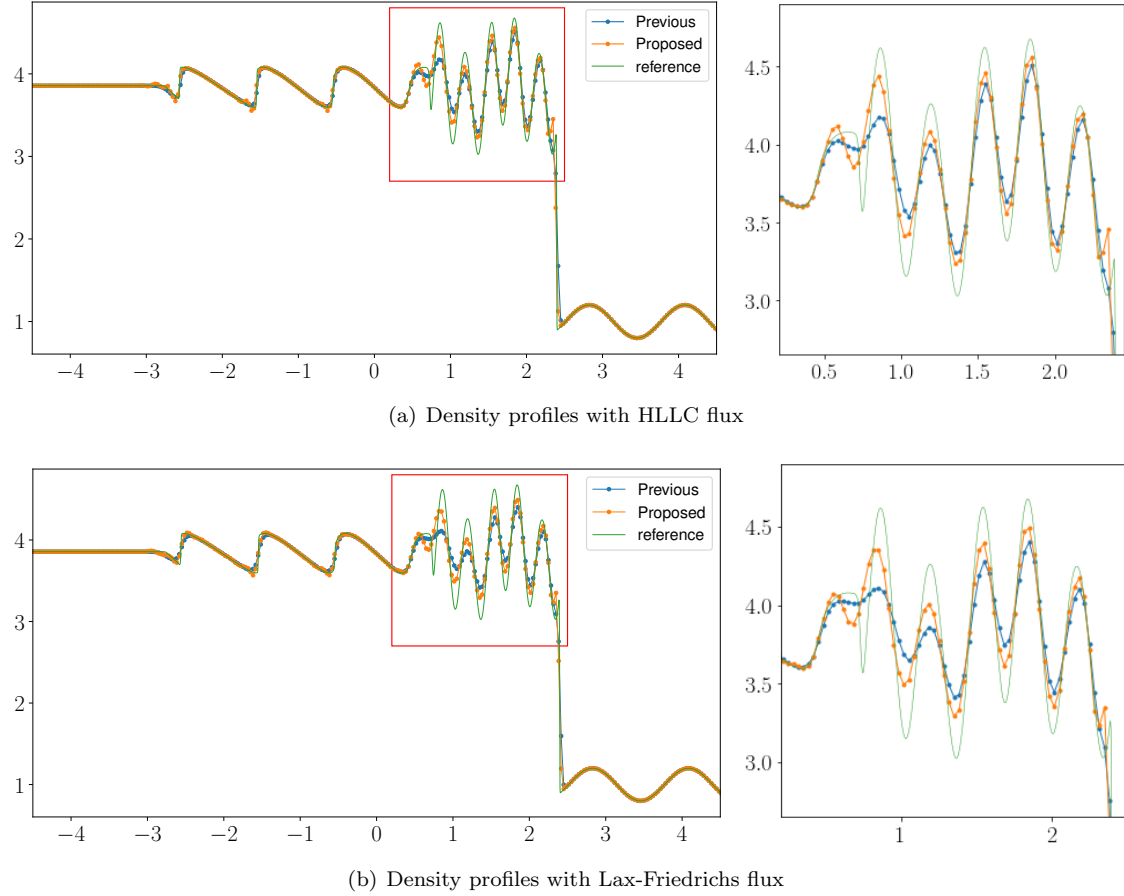


Figure 4: (Example 6.4) Density profiles of the shock-entropy interacting problem [36] at $t = 1.8$, with $\Delta x = 10/300$, using the HLLC flux (a) and the Lax-Friedrichs flux (b).

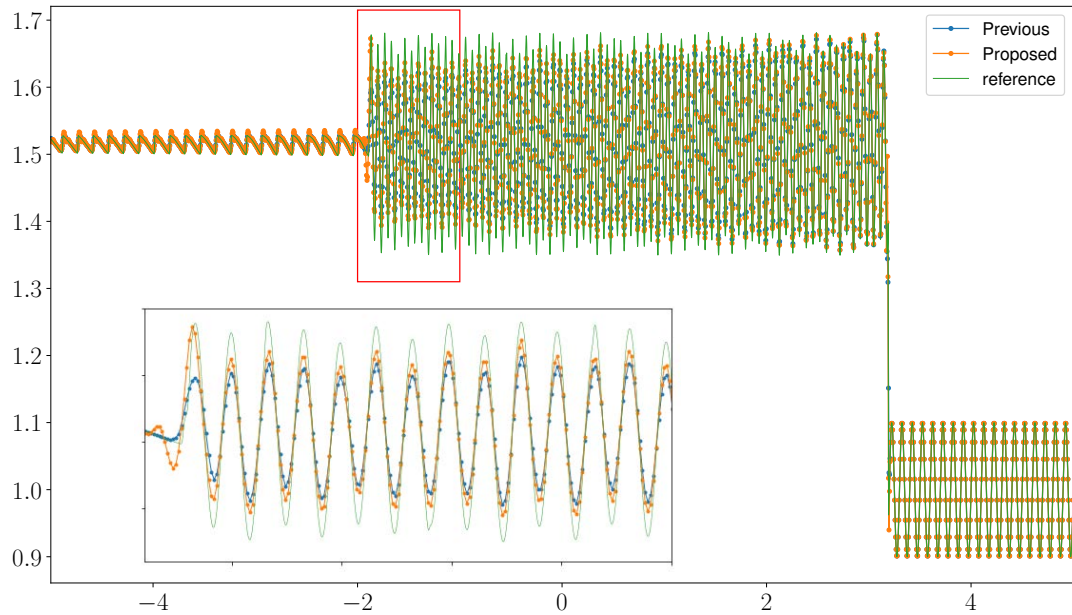


Figure 5: (Example 6.5) Density profiles of the shock-turbulence problem [40] at $t = 5$ with $\Delta x = 1/200$.

6.2 Weakly Hyperbolic System

In this subsection, we consider the more challenging pressureless Euler equation, which, in 1D, is given by

$$U_t + F(U)_x = 0, \quad (36)$$

with

$$U = (\rho, \rho u)^T, \quad F(U) = (\rho u, \rho u^2)^T.$$

Such pressureless systems are important in modeling systems of dilute gases in a vacuum which undergo few collisions. When collisions do occur, they are said to be perfectly inelastic, causing the gas particles to stick together. These collisions lead to the emergence of so-called δ -shocks, which are the primary feature of interest in these models. Note that because the system is weakly hyperbolic, the characteristic decomposition is not available for this problem. Consequently, the simple Lax-Friedrichs flux cannot be directly used in this problem. Instead, we consider the Godunov flux, outlined in [44], which was originally introduced by Bouchut, *et al.* in [53]. Before defining the flux, we remark that the latter work contains a fairly diverse collection of literature on isothermal gas dynamics, so we refer the interested reader to references therein for further details. The former article considered more general problems involving δ -shocks, including the system (36), and applied DG methods to solve such problems. To define the flux, suppose we have left and right numerical approximations $U_l = (\rho_l, \rho_l u_l)^T$ and $U_r = (\rho_r, \rho_r u_r)^T$. Then, the numerical flux is given by

$$h(U_l, U_r)^T = \begin{cases} (\rho_l u_l, \rho_l u_l^2), & \text{if } u_l > 0, u_r > 0, \\ (0, 0), & \text{if } u_l \leq 0, u_r > 0, \\ (\rho_r u_r, \rho_r u_r^2), & \text{if } u_l \leq 0, u_r \leq 0, \\ (\rho_l u_l, \rho_l u_l^2), & \text{if } u_l > 0, u_r \leq 0, v > 0, \\ (\rho_r u_r, \rho_r u_r^2), & \text{if } u_l > 0, u_r \leq 0, v < 0, \\ \left(\frac{\rho_l u_l + \rho_r u_r}{2}, \rho_l u_l^2 = \rho_r u_r^2 \right), & \text{if } u_l > 0, u_r \leq 0, v = 0, \end{cases}$$

where

$$v = \frac{\sqrt{\rho_l} u_l + \sqrt{\rho_r} u_r}{\sqrt{\rho_l} + \sqrt{\rho_r}}.$$

Example 6.6 For our first test, we seek to determine the approximation order for weak hyperbolic system. To this end, we solve pressureless Euler system (36) with the following initial data

$$\rho_0(x) = \sin(x) + 2, \quad u_0(x) = \sin(x) + 2,$$

subject to periodic boundary conditions. The exact solution for this problem is

$$\rho(x, t) = \frac{\rho_0(x_0)}{1 + t u_0'(x_0)}, \quad u(x, t) = u_0(x_0),$$

where x_0 is given implicitly by

$$x_0 + t u_0(x_0) = x.$$

The L_∞ , L_1 and L_2 errors and approximation orders for the density ρ at $t = 0.1$ are given in Table 3. For the classical WENO scheme, we observe a reduction in the convergence order by nearly a factor of two, a phenomena which was also observed in [44]. In contrast, the proposed scheme, which makes use of the non-polynomial basis, achieves the intended accuracy. The shape parameters for the RBF $\phi = e^{-\lambda^2 x^2}$, were computed to first and second order accuracy (i.e., $p = 1$ and $p = 2$ in (19)), which, we have designated the labels “Proposed I” and “Proposed II”, respectively, as in the Example 6.1. These schemes exhibit convergence rates of fifth and sixth order, as shown in Table 3.

Example 6.7 We solve the problem known as two interactive blast wave problem [42] which has the initial data

$$(\rho_0, u_0) = \begin{cases} (1, 1) & \text{if } x < 0, \\ (0.25, 0) & \text{if } x > 0. \end{cases}$$

We compared the classical WENO scheme against the RBF-WENO scheme, which uses fourth order approximations on the local substencils, on a uniform mesh with the cell-spacing $\Delta x = 1/80$. In Figure

	N_x	WENO-JS5	Proposed I	Proposed II
L_∞	20	1.89e-03 (—)	8.38e-04 (—)	7.38e-04 (—)
	40	6.90e-05 (4.77)	1.98e-05 (5.41)	1.32e-05 (5.80)
	80	3.62e-06 (4.25)	5.68e-07 (5.12)	2.12e-07 (5.96)
	160	2.48e-07 (3.87)	1.67e-08 (5.08)	3.37e-09 (5.97)
	320	1.90e-08 (3.71)	5.05e-10 (5.05)	5.30e-11 (5.99)
L_1	20	3.23e-03 (—)	1.95e-03 (—)	1.45e-03 (—)
	40	1.13e-04 (4.84)	4.52e-05 (5.43)	2.41e-05 (5.91)
	80	3.68e-06 (4.94)	1.15e-06 (5.30)	3.81e-07 (5.98)
	160	1.25e-07 (4.88)	3.17e-08 (5.17)	6.04e-09 (5.98)
	320	4.68e-09 (4.74)	9.27e-10 (5.10)	9.47e-11 (5.99)

Table 3: (Example 6.1) L_∞ and L_1 errors and convergence rates(*) at $t = 1$.

6, we plot the density profiles for the two methods at time $t = 0.3$. We observe a δ -shock, in the density, at the location $x = 0.2$. We observe a remarkable difference in the overall height of the shocks predicted by the two approaches. The shock width predicted by the RBF method is also sharper and slightly more narrow than the that predicted by the classical method. To the right of the shock, we also observe some undershoots in the densities predicted by both methods; however, the undershoot in the RBF method is marginally smaller, despite the RBF method's small substencil size. As discussed earlier, reducing the overshoot and undershoot in these rapidly varying transition regions is something we plan to address in our future work.

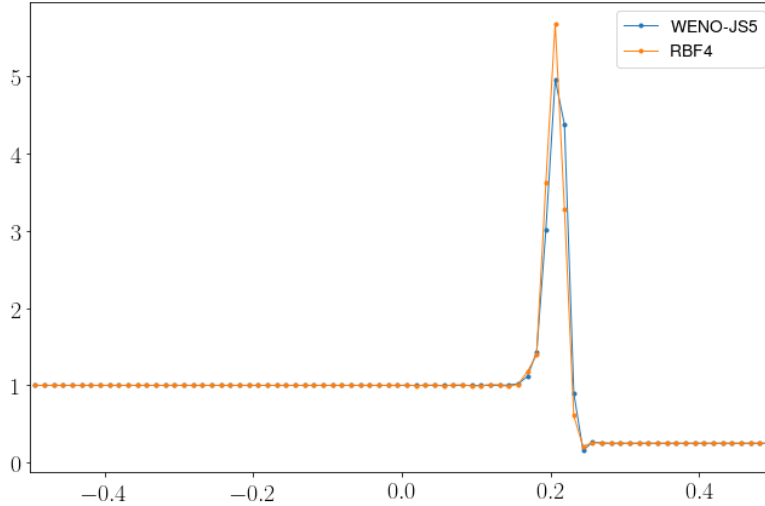


Figure 6: (Example 6.7) Density profiles of δ -shock wave problem [42] at $t = 0.3$ with $\Delta x = 1/80$

7 Conclusion

In this paper, we proposed superconvergent FV RBF-WENO methods which are built on a non-polynomial basis consisting of RBFs. Superconvergence in the interpolation component of the reconstruction was achieved by exploiting the shape parameter in the definition of the RBF. More specifically, by analyzing the error in the reconstructions, we derived expressions for optimal shape parameters which improved the convergence order of the interpolation. While the methods developed in this work considered Gaussian functions, the same techniques can be easily applied to develop schemes based on other RBFs. The proposed schemes, whose constructions make use of fairly compact stencils, incorporate new smoothness indicators which were previously shown to be highly effective at discerning rapid changes in a function. To alleviate the heavy computational cost typically associated with WENO methods, we chose to implement these ideas as part of a hybrid solver that dynamically prescribes the reconstruction method according

to the local smoothness of the function. The proposed schemes were applied to a solve 1D systems of conservation laws and compared against results obtained with a fifth order classical WENO method. While the proposed methods demonstrated improved shock-capturing capabilities over classical WENO approaches, the use of the non-polynomial basis was shown to be particularly effective for problems containing rapid transitions as well as complex wave structures and singularities. Furthermore, in the case of the pressureless Euler equations, the proposed RBF-WENO methods were experimentally shown to achieve their theoretical convergence rates, avoiding the order reduction encountered by standard reconstruction techniques. A highlight of this work is reflected in the blast wave problem (see Example 6.7 in section 6.2), where the proposed RBF method and standard WENO approaches lead to markedly different predictions of the shock. While these results suggest several avenues for future research, we plan to investigate strategies for further reducing oscillations, e.g., around transition regions, as well as extensions of these ideas to include additional spatial dimensions.

Appendices

A Towards a Generalization of Theorem 4.1

Here we provide the following theorem for the cases when N is an odd number for the development of full analysis of proposed scheme.

Theorem A.1 *Let u be a smooth function on Ω and ϕ be a smooth radial basis function. Given a set of reference points $\{x_k \in \Omega : k = 1, \dots, N\}$ for an odd integer N , there exists a set of coefficients $\{\alpha_k : k = 1, \dots, N\}$ of the approximation*

$$Au(x) = \sum_{k=1}^N \alpha_k \phi(x - x_k)$$

to the function $u(x)$, which are constructed from cell averaged data $\{\bar{u}(x_j) : x_j \in \Omega\}$. Furthermore, the approximation can be made $(N+1)$ st order accurate, i.e.,

$$Au(x) = u(x) + \mathcal{O}(\Delta x^{N+1}),$$

for $x \in \Omega$.

We show an example for the case of $N = 3$ on the behalf of the proof of Theorem A.1. Suppose that we construct the approximation of a smooth function u at $x = x_{j+\frac{1}{2}}$ using the cell averages $\{\bar{u}_j : j = -1, 0, 1\}$. Using a primitive function

$$U(x) = \int_{x-\frac{1}{2}}^x u(\xi) d\xi,$$

the approximation using a radial basis function $\phi(x) = e^{-\lambda^2 x^2}$ is defined by

$$AU(x) := \sum_{k=-1}^2 \alpha_k \phi(x - x_{j+k-\frac{1}{2}}),$$

so that $AU'(x) \approx u(x)$. Repeating the steps outlined in subsection 3.1.2, and Taylor expanding the RBF approximation, we find that

$$AU'(x_{j+\frac{1}{2}}) = u(x_{j+\frac{1}{2}}) + \Delta x^3 \left(\lambda^2 u'(x_{j+\frac{1}{2}}) + \frac{1}{12} u'''(x_{j+\frac{1}{2}}) \right) + \mathcal{O}(\Delta x^4).$$

Therefore the third order scheme can be improved to fourth order accuracy through the choice

$$\lambda^2 = -\frac{u'''(x_{j+\frac{1}{2}})}{12u'(x_{j+\frac{1}{2}})} + \mathcal{O}(\Delta x).$$

Acknowledgements. We would like to thank AFOSR and NSF for their support of this work under grants FA9550-19-1-0281 and FA9550-17-1-0394 and NSF grant DMS 191218.

References

- [1] F. Acker, R. B. de R. Borges, and B. Costa, An improved WENO-Z scheme, *J. Comput. Phys.* 313, 726–753 (2016).
- [2] S. Adjerid, K. D. Devine, J. E. Flaherty, and L. Krivodonova, A posteriori error estimation for discontinuous Galerkin solutions of hyperbolic problems, *Comput. Methods Appl. Mech. Engrg.* 191, 1097–1112 (2002).
- [3] S. Adjerid and T. C. Massey, Superconvergence of discontinuous Galerkin solutions for a nonlinear scalar hyperbolic problem, *Comput. Methods Appl. Mech. Engrg.* 195, 3331–3346 (2006).
- [4] D.S. Balsara, S. Garain and C.W. Shu, An efficient class of WENO schemes with adaptive order, *J. Comput. Phys.* 326, 780–804 (2016).
- [5] D.S. Balsara and C.W. Shu, Monotonicity prserving WENO schemes with increasingly high-order of accuracy, *J. Comput. Phys.* 160, 405–452 (2000).
- [6] C. Bigoni and J.S. Hesthaven, Adaptive WENO methods based on radial basis function reconstruction, *J. Sci. Comput.* 72, 986—1020 (2017).
- [7] R. Borges, M. Carmona, B. Costa, and W.S. Don, An improved WENO scheme for hyperbolic conservation laws, *J. Comput. Phys.* 227, 3191–3211 (2008).
- [8] M. D. Buhmann, Radial basis functions, *Acta Numerica* 9, 1–38 (2000)
- [9] Y. Cheng and C. Shu, Superconvergence and time evolution of discontinuous Galerkin finite element solutions, *J. Comput. Phys.* 227, 9612–9627 (2008).
- [10] Y. Cheng and C. Shu, Superconvergence of discontinuous Galerkin and local discontinuous Galerkin schemes for linear hyperbolic and convection-diffusion equations in one space dimension, *SIAM J. Numer. Anal.* 47, 4044–4072 (2010).
- [11] G.A. Gerolymos, D.Sénéchal, and I. Vallet, Very-high-order WENO schemes, *J. Comput. Phys.* 228, 8481–8524 (2009).
- [12] D. Gottlieb, and C.-W. Shu, On the Gibbs phenomenon and its resolution *SIAM Review* 39 (4), 644–668 (1997).
- [13] D. Gottlieb, C.-W. Shu, A. Solomonoff and H. Vandeven, On the Gibbs phenomenon I: recovering exponential accuracy from the Fourier partial sum of a nonperiodic analytic function, *J. Comput. Appl. Math.* 43, 81–98 (1992).
- [14] S. Gottlieb, J. S. Mullen, and S.J. Ruuth, A Fifth Order Flux Implicit WENO Method, *J. Sci. Comput.* 27 (1-3), 271-287 (2006).
- [15] J. Guo and J.-H. Jung A RBF-WENO finite volume method for hyperbolic conservation laws with the monotone polynomial interpolation method, *Applied Numerical Mathematics* 112, 27–50 (2017).
- [16] Y. Ha, C. H. Kim, Y. H. Yang, and J. Yoon, Sixth-order weighted essentially non-oscillatory schemes based on exponential polynomials, *SIAM J. Sci. Comput.* Vol. 38, No. 4, A1987–A2017 (2016).
- [17] Y. Ha, C. H. Kim, Y. H. Yang, and J. Yoon, Construction of an improved third-order WENO scheme with a new smoothness indicator, *J. Sci. Comput.* 82:63 (2020).
- [18] Y. Ha, C. H. Kim, Y. H. Yang, and J. Yoon, Improving accuracy of the fifth-order WENO scheme by using the exponential approximation space, preprint, arxiv:2002.06175, 2020.
- [19] A. Harten, High resolution schemes for hyperbolic conservation laws, *J. Comput. Phys.*, 49, 357–393 (1983).
- [20] A. Harten, On a Class of High Resolution Total-Variation-Stable Finite-Difference Schemes, *SIAM J. Numer. Anal.* Vol. 21, no. 1, 1–23 (1984).
- [21] A. Harten and S. Osher, Uniformly High-Order accurate Non-Oscillatory schemes I. *SIAM J. Numer. Anal.* Vol. 24, No. 2, 279–309 (1987).

- [22] A. Harten, B. Engquist, S. Osher, and S. Chakravarthy, Uniformly High-Order accurate Non-Oscillatory schemes III. *J. Comput. Phys.* 131, 3–47 (1997).
- [23] A.K. Henrick, T.D. Aslam, and J.M. Powers, Mapped weighted-essentially-non-oscillatory schemes : achieving optimal order near critical points, *J. Comput. Phys.* 207, 542–567 (2005).
- [24] X. Y. Hu Q. Wang, and N. A. Adams, An adaptive central-upwind weighted essentially non-oscillatory scheme, *J. Comput. Phys.* 229, 8952–8965 (2010).
- [25] G. Jiang and C.W. Shu, Efficient implementation of weighted ENO schemes, *J. Comput. Phys.* 126, 202–228 (1996).
- [26] Y. Jiang, C.-W. Shu, and M. Zhang, An alternative formulation of finite difference weighted ENO schemes with Lax–Wendroff time discretization for conservation laws, *SIAM J. Sci. Comput.* 35, 1137–1160 (2013).
- [27] S. Karlin and W.J. Studden, *Tchebycheff Systems: With Applications in Analysis and Statistics*, Interscience Publishers, New York, 1966.
- [28] P.D. Lax, Weak solutions of Nonlinear Hyperbolic Equations and their Numerical Computation, *Commun. Pure Appl. Math.* 7, 159–193 (1954).
- [29] X.-D. Liu, S. Osher, and T. Chan, Weighted essentially non-oscillatory schemes, *J. Comput. Phys.* 115, 200–212 (1994).
- [30] S.E. Olson, A.J. Christlieb, Gridless DSMC, *J. Comput. Phys.* 227, 8035–8064 (2008).
- [31] A. Reyes, D. Lee, C. Graziani, and P. Tzeferacos, A new class of high-order methods for fluid dynamics simulations using Gaussian process modeling, *J. Sci. Comput.* 76, 443–480 (2018).
- [32] A. Reyes, D. Lee, C. Graziani, and P. Tzeferacos, A variable high-order shock-capturing finite difference method with GP-WENO, *J. Comput. Phys.* 381, 189–217 (2019).
- [33] S.A. Sarra and E.J. Kansa, Multiquadric radial basis function approximation methods for the numerical solution of partial differential equations, *Adv. Comput. Mech.* 2 (2009).
- [34] S. Serna and A. Marquina, Power-ENO methods: a fifth-order accurate weighted power ENO method, *J. Comput. Phys.* 194, 632–658 (2004).
- [35] C.-W. Shu and S. Osher, Efficient implementation of essentially non-oscillatory shock capturing schemes, *J. Comput. Phys.* 77, 439–471 (1988).
- [36] C.-W. Shu and S. Osher, Efficient implementation of essentially non-oscillatory shock capturing schemes II, *J. Comput. Phys.* 83, 32–78 (1989).
- [37] C.-W. Shu and P.S. Wong, A note on the accuracy of spectral method applied to nonlinear conservation laws, *J. Sci. Comput.* 10 (3), 357–369 (1995).
- [38] G. Sod, A survey of several finite difference methods for systems of nonlinear hyperbolic conservation laws, *J. Comput. Phys.* 27, 1–31 (1978)
- [39] T. Sonar, Optimal recovery using thin plate splines in finite volume methods for the numerical solution of hyperbolic conservation laws, *IMA Journal of Numerical Analysis* 16(4), 549–581 (1996).
- [40] V. A. Titarev and E. F. Toro, Finite-volume WENO schemes for three-dimensional conservation laws, *J. Comput. Phys.* 201, 238–260 (2004).
- [41] E.F. Toro, Riemann Solvers and Numerical Methods for Fluid Dynamics, *Springer-Verlag*, New York, 1997.
- [42] P. Woodward and P. Colella, The Numerical Simulation of Two-Dimensional Fluid Flow with Strong Shocks, *J. Comput. Phys.* 54, 115–173 (1984).
- [43] Z.F. Xu, C.W. Shu, Anti-diffusive flux corrections for high order finite difference WENO schemes, *J. Comput. Phys.* 205, 458–485 (2005).

- [44] Y. Yang, D. Wei, and C.W. Shu, Discontinuous Galerkin method for Krause's consensus models and pressureless Euler equations. *J. Comput. Phys.* 252, (2013), 109–127.
- [45] J. Yoon, Spectral approximation orders of radial basis function interpolation on the sobolev space, *SIAM J. Math. Anal.* Vol. 33, No. 4, 946–958 (2001).
- [46] R. Zhang, M. Zhang, and C.W. Shu, On the order of accuracy and numerical performance of two classes of finite volume WENO schemes, *Commun. Comput. Phys.* 5, 836–848 (2009)
- [47] J. Zhu and J. Qiu, Trigonometric WENO schemes for hyperbolic conservation laws and highly oscillatory problems, *Commun. Comput. Phys.* 8, 1242–1263 (2010).
- [48] J. Zhu and J. Qiu, WENO schemes and their application as limiters for RKDG methods based on Trigonometric approximation spaces, *J. Sci. Comput.* 55, 606–644 (2013).
- [49] J. Zhu and J.X. Qiu, A new fifth order finite difference WENO scheme for solving hyperbolic conservation laws, *J. Comput. Phys.* 318, 110–121 (2016).
- [50] J. Zhu and J.X. Qiu, A new type of finite volume WENO schemes for hyperbolic conservation laws, *J. Sci. Comput.* 73, 1338–1359 (2017).
- [51] S. Gottlieb, C.W. Shu, and E. Tadmor, Strong stability-preserving high-order time discretization methods, *SIAM review* 43, 89–112 (2001).
- [52] J.S. Hesthaven, Numerical Methods for Conservation Laws: From Analysis to Algorithms, *SIAM Computational Science and Engineering* (2018).
- [53] F. Bouchut, S. Jin, and X. Li, Numerical approximations of pressureless and isothermal gas dynamics, *SIAM Journal on Numerical Analysis* 41, 135–158 (2003).